ANNALS OF GEOPHYSICS, 65, 6, RS642, 2022; doi:10.4401/ag-8823
OPEN ACCESS

# The FastVRP automatic platform for the thermal monitoring of volcanic activity using VIIRS and SLSTR sensors

Federica Torrisi[*,1,2], Eleonora Amato[1,3], Claudia Corradino[1], Ciro Del Negro[1]

(1) Istituto Nazionale di Geofisica e Vulcanologia, Osservatorio Etneo – Sezione di Catania, Piazza Roma 2, 95125 Catania, Italy.
(2) Department of Electrical, Electronic and Computer Engineering, University of Catania, Viale Andrea Doria 6, 95125 Catania, Italy
(3) Department of Mathematics and Computer Science, University of Palermo, Via Archirafi 34, 90123 Palermo, Italy

Article history: received March 23, 2022; accepted October 29, 2022

## Abstract

Satellite thermal remote sensing is widely used to detect and quantify the high-temperature volcanic features produced during an eruption, e.g. released radiative power. Some space agencies provide Fire Radiative Power (FRP) Products to characterize any thermal anomaly around the world. In particular, Level-2 FRP Products of the Visible Infrared Imaging Radiometer Suite (VIIRS) and the Sea and Land Surface Temperature Radiometer (SLSTR) are freely available online and they allow to monitor high-temperature volcanic features related to the dynamics of volcanic activity. Here, we propose the FastVRP platform developed in Google Colab to process automatically the FRP Products provided by the National Aeronautics and Space Administration (NASA) and the European Space Agency (ESA) space agencies. FastVRP was designed to monitor the volcanic radiative power (VRP) related to eruptive activity of Mt. Etna (Sicily, Italy). We compared the quality of these FRP Products during a number of recent paroxysmal lava fountains occurred at Etna volcano between February and March 2021. We highlighted the advantages and the limits of each sensor in monitoring intense volcanic eruptions lasting a few hours. Furthermore, we combine the mid-high spatial/low temporal resolution VIIRS and SLSTR with the low spatial-high temporal resolution SEVIRI (Spinning Enhanced Visible and Infrared Radiometer Imager) to improve estimates of the energies released from each paroxysmal episode. In particular, we propose a fitting approach to enhance the accuracy of SEVIRI low spatial-high temporal resolution measurements exploiting the few acquisitions from VIIRS and SLSTR high spatial-low temporal resolution during lava fountain cooling phase. We validated the radiative power values forecasted from VIIRS and SLSTR with the radiative power values retrieved using MODIS (Moderate Resolution Imaging Spectroradiometer) sensor.

Keywords: Volcanic thermal anomalies; Satellite remote sensing; Volcanic radiative power (VRP); Level-2 Product; Geostationary and polar satellites

## 1. Introduction

Satellite remote sensing thermal images have been used to observe volcanoes worldwide for several decades and have been proved to be a valuable and effective tool to detect and quantify thermal anomalies (also called hotspots) associated with volcanic activity. Infrared radiometers on-board of geostationary and polar satellites orbiting around the Earth are used to measure radiance from high-temperature volcanic features [Harris, 2013; Corradino et al., 2019], whose released energetic content is quantified by the radiative power. Firstly, hotspot pixels, i.e. thermally active pixels indicating the presence of a thermal anomaly, are detected by means of different techniques, e.g. spatial-based (or contextual) algorithm [Harris et al., 1995; Higgins & Harris, 1997; Ganci et al., 2012], temporal-based algorithm [Tramutoli, 1998; Di Bello et al., 2004; Pergola et al., 2004], spectral-based (or fixed threshold) algorithm [Wright et al., 2002; Flynn et al., 2002], machine learning techniques [Piscini & Lombardo, 2014; Corradino et al., 2022]. Then, the radiative power released by thermal anomalies can be estimated using the middle infrared (MIR) radiance technique proposed by Wooster et al. [2003], according to which the energy emitted by a hot surface, i.e. temperature greater than 500K, is directly related to its satellite measured radiance at about 4 μm.

Numerous volcanic hotspot monitoring platform were developed for the near real-time monitoring of thermal anomalies using satellite data, such as MODVOLC [Wright et al., 2004], HOTVOLC [Gouhier et al., 2016], FIRMS [Davies et al., 2019], MIROVA [Coppola et al., 2020] and LAV@HAZARD [Vicari et al., 2011]. In particular, the last two platforms are able to provide a complementary information because of the different temporal and spatial resolutions of sensors used, namely MODIS (Moderate Resolution Imaging Spectroradiometer) in MIROVA and SEVIRI (Spinning Enhanced Visible and Infrared Radiometer Imager) in LAV@HAZARD. MODIS, onboard Aqua and Terra polar satellites, provides data four times per day with a spatial resolution from 250 to 1000 m, but a low temporal resolution (about 2 acquisitions per day); on the other hand, SEVIRI, onboard the geostationary Meteosat Second Generation (MSG) satellites, has a coarse spatial resolution (about 3 km at the equator), but this is balanced by its high temporal resolution (up to one sample every five minutes in rapid scan mode for North Africa and Central Europe). MIROVA uses MODIS data to detect, locate and quantify thermal anomalies in near real-time (https://www.mirovaweb.it/). The hotspot detection algorithm implemented in MIROVA exploits both spatial and spectral information, in particular the MIR bands at 3.959 μm and thermal infrared (TIR) bands at 12.02 μm are used to detect the presence of hot objects inside the pixels. Once the hot pixels have been identified, the radiative power is calculated using the MIR radiance technique. LAV@HAZARD is a web-GIS platform for volcanic hazard assessment, based on the analysis of infrared data acquired by SEVIRI. LAV@HAZARD uses a contextual algorithm to detect volcano thermal anomalies and, for each hotspot pixel, the radiative power is calculated using the MIR radiance technique. SEVIRI enables the monitoring of short and rapidly evolving eruptive phenomena, e.g., lava fountains which have a duration of a few hours [Hirn et al., 2008; Lombardo et al., 2019]. Generally, lava fountains feed several-km high eruptive columns and ash plumes, as well as short-lived lava flows. The thermal waveform during a lava fountain is made by an initial phase of sharp increase in heat fluxes, which reach a peak corresponding to the main fountaining activity, and a subsequent phase characterized by waning heat flux associated with the slow cooling of the lava overflowed from the crater rim. This thermal behavior is described by the so-called cooling curve [Ganci et al. 2012]. High temporal resolution thermal data, like SEVIRI data, are well suited to characterize these cooling curves, which follow a fountaining event and decay within a few hours. As it is discussed in Ganci et al. [2012], fitting the general shape of a cooling curve and applying an algorithm of best fit, determined by minimizing the mean squared error between the modelled radiative heat fluxes and the measured heat flux curve, it is possible to obtain an estimation of the area covered by the lava flow. Sensors used for a more accurate estimate of the lava flow area are those having a good spatial resolution, like the MultiSpectral Instrument (MSI, 10-m bands) on board of Sentinel-2 satellite, the Operational Land Imager (OLI, with 30-m bands) and the Thermal Infrared Sensor (TIRS, with 100-m bands) on board Landsat-8 satellite, or the Advanced Spaceborne Thermal Emission and Reflection Radiometer (ASTER, 15-m to 90-m bands), onboard Terra satellite [Li et al., 2017; Corradino et al., 2019; Corradino et al., 2021; Amato et al., 2021]. The development of algorithms exploiting multi-sensor data for monitoring and quantifying thermal volcanic activity has allowed to get more accurate results over time [Ganci et al., 2016; Marchese et al., 2019; Valade et al., 2019; Massimetti et al., 2020].

Nowadays, space agencies make available processed satellite data free of charge. In particular, specific geophysical parameter values are usually derived using models and auxiliary datasets, these are named Level-2 products. Among the Level-2 products, fire radiative power (FRP) measures the rate at which a thermally active area is emitting radiative energy. In particular, the National Aeronautics and Space Administration (NASA) and the European Space

Agency (ESA) space agencies provide FRP Level-2 products derived respectively from the Visible Infrared Imaging Radiometer Suite (VIIRS) and the Sea and Land Surface Temperature Radiometer (SLSTR). Only recently VIIRS FRP Product has been used to monitor volcanic activity because of its improved spatial resolution, up to 375 m [Gunda et al., 2021; Campus et al., 2022], while SLSTR has not been used yet for this purposes even though it has a comparable temporal resolution with respect to MODIS but a higher saturation temperature at MIR and TIR bands.

Here, we propose a new platform in Google Colab, called FastVRP, to analyze changes of Volcanic Radiative Power (VRP) emitted by active volcanoes, using Level-2 FRP Products. We explore the potentiality of these products retrieved from VIIRS and SLSTR data, in detecting and quantifying the thermal output from the Etna volcano (Sicily, Italy) during the sequence of intense lava fountains occurred between February and April 2021. Moreover, a novel approach to forecast the thermal behavior of a lava fountain and then to reconstruct its cooling curve from the low temporal resolution VRP values is proposed. This procedure is performed outside the Google Colab platform, but exploits the data provided by FastVRP. It is based on the combination of the temporal features provided by the geostationary satellite sensor SEVIRI and the accurate spatial features provided by the two polar satellite sensors, VIIRS and SLSTR. We validated this approach exploiting the radiative power estimated from MODIS, having features similar to those of VIIRS and SLSTR sensors.

# 2. Materials

## 2.1 Record of the lava fountain events

Since the beginning of the new millennium, the eruptive activity of Mt. Etna (Figure 1) is dominated by sequences of lava fountain events, mostly occurring from the South-East Crater (SEC) located in the summit area.

Generally, paroxysmal episodes taking place close in time are impulsive and characterized by rapid waxing and waning phases compared to the episodes more distant in time showing a slower pattern [Andronico et al., 2021]. The first relevant sequence occurred in 2000, when the SEC produced 64 episodes [Alparone et al., 2003], followed by explosive phases occurred in 2001 [Behncke & Neri, 2003], 2002-2003 [Andronico et al., 2008], and 2011-2015 [Ganci et al. 2018]. The last explosive phase started on 13 December 2020 and ended on 21 February 2022, giving rise to 66 paroxysmal lava fountain episodes from SEC [Calvari & Nunnari, 2022]. Lava fountains were significantly more intense and frequent between mid-February and early April 2021. This short period of time was characterized by a sequence of 17 paroxysms of short duration (a few hours) and high intensity, occurred with a certain regular frequency (every about 30 hours from each other). These events are listed in Table 1 as identified by the INGV weekly bulletins published at www.ct.ingv.it. Most of these lava fountains were associated with several km high ash plumes (up to 9-10 km above sea level), generating serious concern among the population living in towns located around

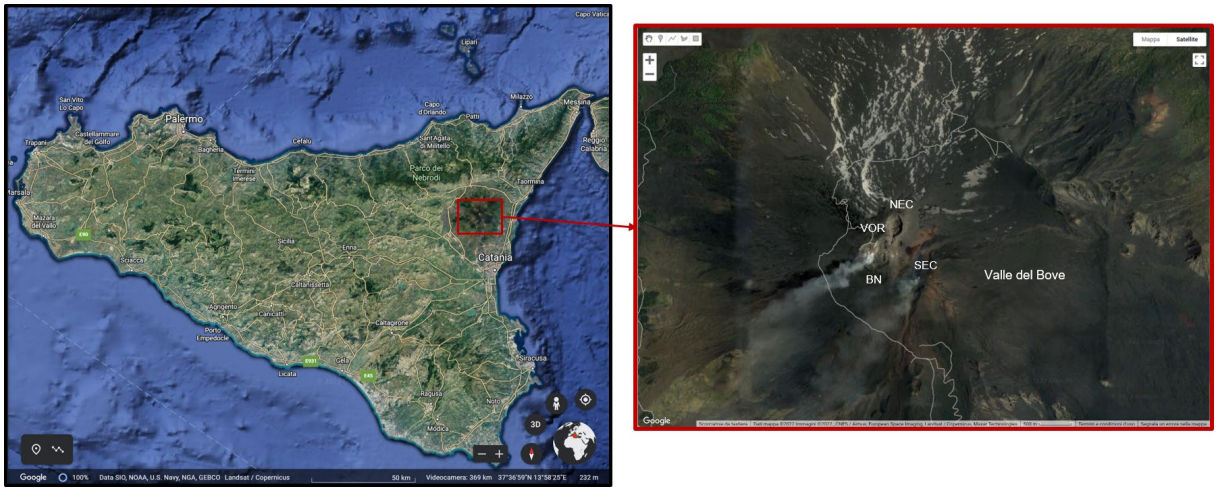


**Figure 1.** Mt. Etna volcano in Sicily, and relative summit area (red box), with four summit craters, the Voragine (VOR), the Bocca Nuova (BN), the Northeast Crater (NEC), and the Southeast Crater (SEC), and the Valle del Bove.

the volcano [Torrisi, 2022]. The impact of ash fallout was quite strong on the air traffic, on the stability of roofs, and on the health of the population living near the volcano [Andronico & Del Carlo, 2016; Torrisi et al., 2022]. In addition, pyroclasts and the small lava flows erupted during the lava fountains represented the greatest hazards to the tourist facilities on the upper flanks of Etna [Corradino et al., 2021; Amato, 2022].

| Number | Event | Start Time | End Time | Time duration | Max height lava fountains |
|---|---|---|---|---|---|
| 1 | 16 February 2021 | 17:05 UTC | 18:00 UTC | 45 min | 1500 m |
| 2 | 17-18 February 2021 | 22:30 UTC | 00:40 UTC | 35 min | 1200 m |
| 3 | 19 February 2021 | 07:55 UTC | 10:10 UTC | 65 min | 1300 m |
| 4 | 20-21 February 2021 | 20:00 UTC | 01:20 UTC | 180 min | 1500 m |
| 5 | 22-23 February 2021 | 20:30 UTC | 10:38 UTC | 50 min | 3600 m |
| 6 | 24-25 February 2021 | 16:00 UTC | 22:20 UTC | 140 min | 1800 m |
| 7 | 28 February 2021 | 08:10 UTC | 09:33 UTC | 54 min | 3600 m |
| 8 | 2-3 March 2021 | 10:45 UTC | 14:50 UTC | 120 min | 600 m |
| 9 | 4 March 2021 | 00:20 UTC | 08:30 UTC | 130 min | 3200 m |
| 10 | 7 March 2021 | 00:00 UTC | 14:00 UTC | 60 min | 4000 m |
| 11 | 9-10 March 2021 | 18:00 UTC | 03:30 UTC | 163 min | 1860 m |
| 12 | 12 March 2021 | 03:20 UTC | 10:00 UTC | 175 min | 2400 m |
| 13 | 14-15 March 2021 | 20:10 UTC | 02:50 UTC | 170 min | 1300 m |
| 14 | 17-18 March 2021 | 00:30 UTC | 06:00 UTC | 170 min | 1500 m |
| 15 | 19 March 2021 | 06:34 UTC | 11:20 UTC | 120 min | 600 m |
| 16 | 23-24 March 2021 | 19:05 UTC | 11:55 UTC | 480 min | 1300 m |
| 17 | 31 March – 1 April 2021 | 23:00 UTC | 08:00 UTC | 540 min | 630 m |

**Table 1.** Paroxysms occurred at Mt. Etna between February and April 2021.

## 2.2 Satellite data sources

The VRP values retrieved in this study are based on the outputs of the Level-2 active FRP Products from VIIRS and SLSTR, and radiometric measurements from SEVIRI and MODIS, derived from LAV@HAZARD.

SEVIRI sensor is the main payload of the current MSG geostationary satellite operated by EUMETSAT (European Organization for the Exploitation of Meteorological Satellites). It has the capacity to observe the Earth in 12 spectral channels covering the visible to the infrared spectral region, with a baseline repeat cycle of 15 minutes (four full disk images per hour) and a 3 x 3 km nominal spatial resolution at the sub-satellite point. MODIS is an instrument aboard the Terra and Aqua satellites, which view the entire Earth's surface every 1 to 2 days. It acquires data in 36 spectral bands and has a spatial resolution from 250 m to 1 km.

### 2.2.1 Level-2 FRP Products

The VIIRS sensor is aboard two satellites: Suomi National Polar-orbiting Partnership (Suomi NPP) and National Oceanic and Atmospheric Administration-20 (NOAA-20). Suomi NPP and NOAA-20 were respectively the first and the second in a series of four Joint Polar Satellite System (JPSS) satellites, a collaborative mission between NOAA and

NASA. They are satellites with a sun-synchronous near-circular polar orbit, located at an altitude of about 833 km. NOAA-20 has the same orbit of Suomi NPP, but is separated in time and space by 50 minutes, providing additional VIIRS coverage [LP DAAC-VIIRS Overview]. Suomi NPP crosses the equator at about 1:30 a.m. and 1:30 p.m., whereas NOAA-20 crossing at 12:40 a.m. and 12:40 p.m.

The 3000 km swath width of VIIRS allows a coverage with no gaps near the equator, with a scan angle range of ±56.28° from nadir [Cao et al., 2013]. VIIRS provides 22 spectral bands at two spatial resolutions: 16 moderate-resolution bands (M-Bands) with a spatial resolution of 750 m at nadir, 5 imaging resolution bands (I-Bands) with a 375 m spatial resolution at nadir, and one panchromatic Day-Night Band (DNB), with a near constant 750 m spatial resolution throughout the scan. Generally, the M-Bands have a better signal-to-noise ratio than the I-Bands.

The VIIRS Level-2 active fire products are distributed by LANCE/FIRMS (Land Atmosphere Near-real-time Capability for EOS / Fire Information for Resource Management System) platform (https://firms.modaps.eosdis.nasa.gov/). The attribute fields for VIIRS active fire products include for each active pixel its latitude and longitude, the brightness temperature of the MIR bands, the acquisition time and acquisition date, the satellite, the scan, the track, the confidence, and the fire radiative power in MW. The active fire detection algorithm uses a multi-spectral contextual algorithm to identify thermal anomalies [Schroeder et al., 2014]. It is based on the complementary use of the I-Bands and M-Bands. The improved spatial resolution of the I-Bands (375 m) increases the capability of the sensor to detect thermally active areas of relatively small size. The bands used for the hotspot detection are the MIR band I4 (spectral range: 3.55-3.93 µm) and TIR band I5 (spectral range: 10.5-12.4 µm). In presence of I4-band saturation, the I-Bands are replaced by the M-Bands, in particular the MIR band M13 (spectral range: 3.97-4.13 µm) and TIR band M15 (spectral range: 10.26-11.26 µm).

The SLSTR sensor is an instrument carried by the European Sentinel-3 satellites, onboard Sentinel-3A and Sentinel-3B, which are part of the Copernicus Programme operated by ESA and EUMETSAT. Each Sentinel-3 satellite has a near-polar and sun-synchronous orbit, with an altitude of about 814 km, and crosses the equator at 10:00 a.m. and 10:00 p.m. [Sentinel-3 – Mission Summary].

The SLSTR uses two independent scan chains, including a separate scan mirror. This configuration is employed to provide a dual-view of the same position of the Earth, "near nadir" and "oblique" [Xu et al., 2021]. The oblique view has a local zenith angle close to 55° and a width of the nominal image swath equal to 740 km, while the nadir view is almost vertical at the sub-satellite point and has a wider swath width than the oblique view, equal to 1400 km. SLSTR has 11 bands: 3 bands in the visible and near-infrared (VNIR) and 3 bands in the short-wave infrared (SWIR) with a spatial resolution of 500 m at nadir, and 5 bands in the thermal infrared (TIR) with a spatial resolution of 1000 m at nadir.

The SLSTR Level-2 active fire products are distributed by Copernicus Open Access Hub (https://scihub.copernicus.eu/). The attribute fields for SLSTR active fire products include for each active pixel its latitude and longitude, the brightness temperature of the MIR bands, the detection time, the confidence, and the fire radiative power in MW. The SLSTR active fire product is derived from data collected in the SLSTR near-nadir view swath since this offers finer spatial detail and a wider swath width than the oblique view. The active fire detection algorithm uses a contextual algorithm to identify thermal anomalies [Wooster et al., 2012; Xu et al., 2020]. The two MIR channels extremely sensitive to the presence of fire exploited are the S7 channel (central wavelength: 3.74 µm) and the low-gain "fire channel" F1 (central wavelength: 3.74 µm). F1 channel is used when the S7 channel saturates, in fact it is able to measure brightness temperatures in excess of 450 K. Furthermore, the TIR bands used for the detection of thermal anomalies are the S8 channel (central wavelength: 10.8 µm) and the F2 channel (central wavelength: 10.8 µm), which is able to measure higher brightness temperature than the standard S8 channel, although this last band saturates rarely. The saturation temperature of the S8 channel is 321 K, while for the F2 channel is 400 K.

Table 2 shows the comparison between VIIRS and SLSTR in sensing geometry and in the algorithm used for active fire characterization. The VIIRS and SLSTR Level-2 FRP Products depend on the characteristics of the sensors themselves (i.e. spatial resolution, scan angle, minimum detection limit, overpass time), the techniques used to detect the thermal anomalies and the algorithms implemented to derive the FRP values. These sensors are onboard polar satellites and acquire about two images per day, but these two sensors do not have a similar overpassing time. The pixel areas of the VIIRS's bands (375 m I-Bands and 750 m M-Bands) are smaller than that of SLSTR (with a spatial resolution of 1000 m), therefore this means that VIIRS has an improved active fire detection capability because it is able to find smaller thermal anomalies [Zhang et al., 2017]. In both cases, thermal anomalies are identified using a contextual algorithm which exploits MIR and TIR bands. A hotspot detection algorithm relies on three different steps, i.e. detection of potential active pixels, background characterization and active

pixel confirmation. They are common to the two sensors but differ in how the thresholds are set and in the size of the background windows. Finally, the VRP of each hotspot pixel is calculated using the MIR radiance approach of Wooster et al. [2003]:

$$VRP = \frac{A_{pixel} \cdot \sigma \cdot \varepsilon}{\alpha \cdot \varepsilon_{MIR} \cdot \tau_{MIR}} \left(L_{MIR} - L_{MIR,bg}\right) \quad (1)$$

| Sensor parameters | | VIIRS | SLSTR |
|---|---|---|---|
| **Orbit altitude** | | ~ 830 km | ~ 814 km |
| **Equator crossing time** | | **Suomi NPP**:<br>1:30 a.m. (descending node)<br>1.30 p.m. (ascending node)<br>**NOAA-20:**<br>12:40 a.m. (descending node)<br>12.40 p.m. (ascending node) | **Sentinel-3A & Sentinel-3B:**<br>10:00 a.m. (descending node)<br>10:00 p.m. (ascending node) |
| **Scan angle** | | ±56.28° | 55° (oblique view)<br>0° (nadir view) |
| **Swath width** | | ~ 3000 km | ~ 740 km (oblique view)<br>~ 1400 km (nadir view) |
| **Fire detection bands and saturation temperature** | **MIR** | I4 (3.55-3.93 µm)<br>saturation: 367 K<br>spatial resolution: 375 m | S7 (3.74 µm)<br>saturation: 311 K<br>spatial resolution: 1000 m |
| | | M13 (3.97-4.13 µm)<br>saturation: 634 K<br>spatial resolution: 750 m | F1 (3.74 µm)<br>saturation: 500 K<br>spatial resolution: 1000 m |
| | **TIR** | I5 (10.5-12.4 µm)<br>saturation: 380 K<br>spatial resolution: 375 m | S8 (10.8 µm)<br>saturation: 321 K<br>spatial resolution: 1000 m |
| | | M15 (10.26-11.26 µm)<br>saturation: 363 K<br>spatial resolution: 750 m | F2 (10.8 µm)<br>saturation: 400 K<br>spatial resolution: 1000 m |
| **Active fire detection algorithm** | | VIIRS active fire detection algorithm [Schroeder et al., 2014] | SLSTR active fire detection algorithm<br>[Wooster 2012, Xu et al., 2020] |
| **FRP calculation**<br>Based on the MIR radiance approach of Wooster et al. [2003] | | VIIRS-I<br>$\alpha = 3.21 \cdot 10^{-9}$ W·m$^{-2}$·sr$^{-1}$·µm$^{-1}$·K$^{-4}$<br>VIIRS-M<br>$\alpha = 2.87 \cdot 10^{-9}$ W·m$^{-2}$·sr$^{-1}$·µm$^{-1}$·K$^{-4}$<br>[Zhang et al., 2017] | $\alpha = 3.30 \cdot 10^{-9}$ W·m$^{-2}$·sr$^{-1}$·µm$^{-1}$·K$^{-4}$<br>[Xu et al., 2021] |

**Table 2.** Comparison between VIIRS and SLSTR in Sensing Geometry and the Algorithm used for active fire characterization.

where $L_{MIR}$ and $L_{MIR,bg}$ are respectively the spectral radiance ($W \cdot m^{-2} \cdot sr^{-1} \cdot \mu m^{-1}$) of the hot pixels and the nonfire background pixels recorded in the MIR band, $A_{pixel}$ is the pixel area ($km^2$), σ is the Stefan-Boltzmann constant ($5.67 \cdot 10^{-8}$ $W \cdot m^{-2} \cdot K^{-4}$), $\tau_{MIR}$ is the atmospheric transmittance in the MIR band, ε is the emissivity, $\varepsilon_{MIR}$ the surface spectral emissivity in the MIR band, and finally α ($W \cdot m^{-2} \cdot sr^{-1} \cdot \mu m^{-1} \cdot K^{-4}$) is a constant. α is determined from empirical best-fit relationships between the blackbody temperature and emitted spectral radiance at 4 µm, based on the approximation of the Stefan's law with the fourth power of the emitter temperature [Wooster et al., 2003]. This constant α depends on the specific sensor employed and the different values for each sensor is reported in Table 2.

# 3. Methods

## 3.1 FastVRP platform

FastVRP is an entry-level, cloud-based platform that leads to an automatic and fast retrieve and process of Level-2 FRP Products to detect and measure the heat radiation released during volcanic activity (Figure 2). The FastVRP platform is based on Google Colaboratory (Colab for short), a free cloud computing platform that allows multiple users to easily share and execute python code through the browser. This environment runs entirely in cloud, providing many pre-installed libraries and dedicated graphical processing units (GPUs) that accelerate the execution of the code.

VRP values are retrieved by using Level-2 FRP Products derived from VIIRS and SLSTR. In particular, VIIRS active fire data are accessed from Earthdata LANCE (https://earthdata.nasa.gov/earth-observation-data/near-real-time), which provide a variety of data products within 3 hours from satellite observation. LANCE distributes Near Real-Time (NRT) active fire data from VIIRS. SLSTR active fire data, instead, are downloaded from the Copernicus Open Access Hub, a portal developed in collaboration with the ESA, which allows access to all users for the Sentinel data products (https://www.copernicus.eu/en).

The process of retrieving data from these space agency portals is quite slow and time-consuming, because the user has to download the products manually, selecting them one by one. By using Google Colab, FastVRP speeds up and automates the data downloading processes. We have used Application Programming Interface (APIs) to do the request to remote web server for retrieving active fire data. Earthdata APIs are used to access data stored in NASA's LANCE; moreover, the FastVRP platform exploits the python package "sentinelsat" that makes searching,

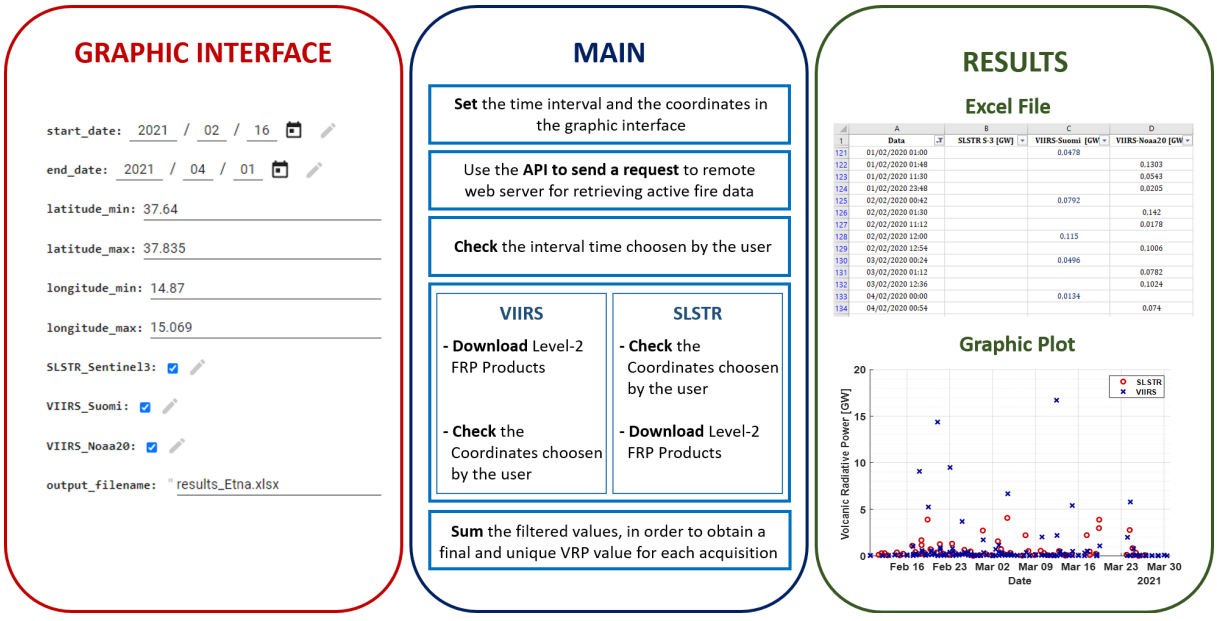


**Figure 2.** Scheme of the FastVRP platform developed in Google Colab, with the graphic interface, the main functions implemented to download automatically the Level-2 FRP Products and the results section, characterized by a file Excel and a graphic plot.

downloading and retrieving the metadata of Sentinel satellite images from the Copernicus Open Access Hub easy, thanks to a powerful Python API (https://sentinelsat.readthedocs.io/en/stable/).

FastVRP has a graphic interface, which gives to the user the possibility to choose the time period to investigate, to set the coordinates of the region of interest, to decide what types of products to download by ticking the appropriate check boxes and to set the name of the file in which the downloaded data will be stored. Once these input parameters are set, FastVRP sends a request to the specific server to download the Level-2 FRP Products, which are automatically saved in the user Google Drive account. Each VIIRS and SLSTR Product contains the information related to all the thermal anomalies detected, including the latitude, the longitude, the acquisition time, and the fire radiative power (in MW).

These data are filtered according to the time period and the coordinates chosen by the user, and the fire radiative power of each pixel of the selected area is summed in order to obtain a final and unique value of VRP for each acquisition. As result, FastVRP generates a data file with all the VRP values related to the sensors selected at the beginning, arranged in chronological order, and a graph in which these radiative power estimates are plotted.

## 3.2 Forecasting of thermal behavior of lava fountains

VIIRS and SLSTR sensors are onboard polar satellites and therefore they acquire images about two times a day. For this reason, VRP values derived from these sensors are not enough to follow accurately the temporal evolution of lava fountain events (lasting few hours). We propose a procedure to forecast missing values by exploiting SEVIRI data at higher temporal resolution.

The SEVIRI radiative power values are able to follow comprehensively the thermal behavior of lava fountains, as shown in Figure 3, thanks to the high sampling rate of the sensor (15 minutes). Since the cooling phase of lava fountains is characterized by an exponential decay of VRP values, we fit with an exponential function the SEVIRI radiative power values in order to estimate the time constant associated with the exponential decay of the measured curve, that is characteristic of each monitored lava fountain event. Starting from the assumption that the time constant characteristic of the lava fountain is not dependent on the sensor but on the physical event, we reconstruct the cooling curve for the low-temporal resolution satellite sensors, i.e. VIIRS and SLSTR, by fitting the few VRP values available. The exponential function used for the fitting is the following:

$$f = f_0 \cdot e^{-\frac{t}{\tau}} \tag{2}$$

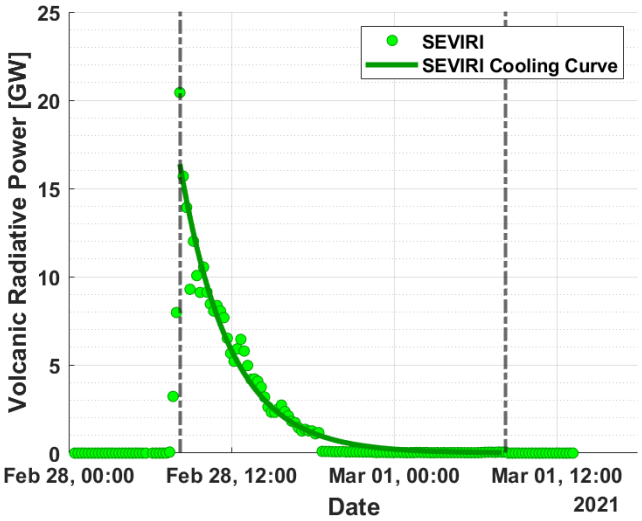


**Figure 3.** Radiative power estimated from SEVIRI data during the lava fountain that occurred on 28 February 2021. The green line indicates the cooling curve obtained fitting the SEVIRI radiative power values, while dotted gray lines specify the peak (on the left) and the end of the eruptive activity (on the right).

where $f_0$ is the initial value (at time t=0) while τ is the exponential decay time constant. Therefore, from the exponential fitting of SEVIRI data, it is possible to obtain the time constant τ related to each paroxysm occurred in the period analyzed (Figure 3).

To reconstruct the cooling curves related to VIIRS and SLSTR VRP values, we need the exponential time constant τ and the initial value $f_0$, which can be estimated starting from the knowledge of τ and taking into account the few VRP values available for each sensor. Generally, two VRP values are used to calculate the initial value $f_0$, but in cases where (a) only a value is acquired, (b) the second acquisition is too far from the peak of the activity (more than two-thirds of the eruptive interval time range) or (c) falls within the first half of the interval time range but takes too low values (<0.5 GW), only the first VRP value is considered to estimate $f_0$. The advantage of using SEVIRI lies in the fact that the forecasting procedure can always be applied, as long as there is at least one VIIRS or SLSTR acquisition. It does not matter if the acquisitions are close to the peak of the activity or far away. If they occur far from the peak of the activity and during the cooling phase, it seems difficult to forecast the thermal activity of the initial phase of the lava fountain. But thanks to the high accuracy of the temporal features provided by SEVIRI, it is however possible to reconstruct of the VIIRS and SLSTR cooling curves precisely.

Taking two VRP values related to the VIIRS sensor ($f_{(1,VIIRS)}$, $f_{(2,VIIRS)}$), the instants they are acquired ($t_{(1,VIIRS)}$, $t_{(2,VIIRS)}$) and the exponential decay factor τ, we can estimate the initial value $f_{(0,VIIRS)}$ using Eq. (3):

$$f_{(0,VIIRS)} = \frac{f_{(1,VIIRS)} + f_{(2,VIIRS)}}{e^{-\frac{t_{(1,VIIRS)}}{\tau}} + e^{-\frac{t_{(2,VIIRS)}}{\tau}}} \tag{3}$$

The same procedure is applied to estimate the initial value $f_{(0,SLSTR)}$ for the SLSTR data:

$$f_{(0,SLSTR)} = \frac{f_{(1,SLSTR)} + f_{(2,SLSTR)}}{e^{-\frac{t_{(1,SLSTR)}}{\tau}} + e^{-\frac{t_{(2,SLSTR)}}{\tau}}} \tag{4}$$

Moreover, given the technical similarity between the VIIRS and SLSTR sensors, in order to increase the number of data points to fit, the cooling curve of the lava fountains is also reconstructed considering a VIIRS value and a SLSTR value; in this case, we take into account the first VIIRS and the first SLSTR acquisition and we calculate the initial value $f_{(0,VIIRS\&SLSTR)}$ as follows:

$$f_{(0,VIIRS\&SLSTR)} = \frac{f_{(1,VIIRS)} + f_{(1,SLSTR)}}{e^{-\frac{t_{(1,VIIRS)}}{\tau}} + e^{-\frac{t_{(1,SLSTR)}}{\tau}}} \tag{5}$$

The reconstruction of the cooling curves allows us to have an estimation of the radiative power for the entire duration of the eruptive event also for sensors like VIIRS and SLSTR that acquire only 2 data per day, and then to forecast the thermal behavior of lava fountains with higher spatial accuracy exploiting the temporal information of sensors like SEVIRI.

To validate the proposed approach for the reconstruction of cooling curves from VIIRS and SLSTR data, we use the radiative power estimated from MODIS data and retrieved from LAV@HAZARD. The finer spatial resolution (i.e. 1 km pixels), the good spectral resolution and the high signal to noise ratio of MODIS enable the identification of less intense thermal anomalies and to locate them with more detail. The MODIS radiative power values for the events analyzed are compared with the radiative power extracted from the cooling curves related to VIIRS and SLSTR at the same observation time of MODIS. What we expect is that if the MODIS point falls in the proximity of the VIIRS and SLSTR cooling curves (or even if it is located above the curve), this means that the physical phenomenon of cooling has been successfully modeled.

The steps for the forecasting of thermal behavior of lava fountains are summarized below:

- fitting of SEVIRI radiative power values and calculation of the exponential decay time constant τ;
- reconstruction of the cooling curves related to VIIRS and SLSTR VRP values exploiting the constant τ and two (or one) VRP values for each sensor;
- validation of the procedure comparing the results with MODIS radiative power values.

## 4. Results

To match the VRP time series retrieved at Mt. Etna during the entire 2021 from VIIRS ($VRP_{VIIRS}$) and SLSTR ($VRP_{SLSTR}$), we calculated for each dataset the weekly mean. Results are shown in Figure 4a, on a logarithmic scale. Moreover, the two weekly datasets have been correlated using a linear regression analysis (Figure 4b). The obtained best-fit coefficient $m = 0.81$ indicates a good correlation between the time series of $VRP_{VIIRS}$ and $VRP_{SLSTR}$.

The temporal trend of radiative power recorded at Mt. Etna during the time span from February to April 2021 is shown in Figure 5. The VRP values from the VIIRS and SLSTR Level-2 Products were retrieved with the FastVRP platform, and the radiative power estimated using SEVIRI data were retrieved from LAV@HAZARD.

We forecasted the thermal behavior of the 17 paroxysms occurred at Mt. Etna between February and April 2021. All the paroxysms were characterized by lava fountains of short duration and high intensity. However, for some events it was not possible to measure the temporal thermal behavior because the cooling curves were not well defined due to missing data. This was caused either by the fact that the cooling process lasted only a few hours or by the presence of adverse weather conditions during the paroxysmal episode that did not allow to process data correctly. Thus, the four paroxysmal events occurred on 10, 15, 17 and 19 March 2021 were not investigated. The results obtained for the other thirteen paroxysmal events analyzed are collected in Table 3. It contains the time interval used for the fitting of SEVIRI radiative power values, the exponential decay factor τ and the initial values $f_{(0,SEVIRI)}$ obtained as results of the fitting procedure and the initial values $f_{(0,VIIRS)}$, $f_{(0,SLSTR)}$, and $f_{(0,VIIRS\&SLSTR)}$ estimated from the knowledge of τ. The symbol (*) indicates that the estimation of $f_0$ was conducted using only a unique VRP value.

As case studies, we considered the three events occurred on 16 February 2021, 20-21 February 2021 and 24-25 February 2021. The reconstructed cooling curves related to VIIRS, SLSTR and combining VIIRS and SLSTR data (VIIRS&SLSTR) are shown in Figures 6-8. For all cases, the initial time, which corresponds to the peak of the

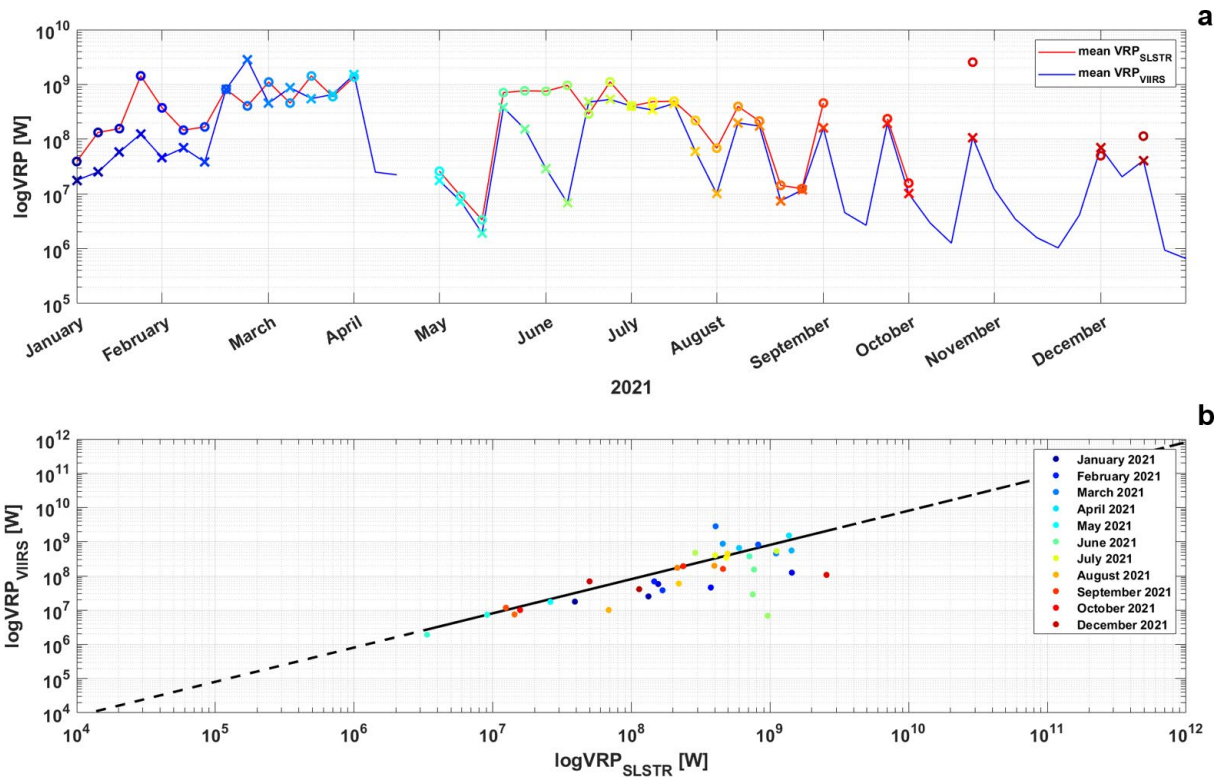


**Figure 4.** (a) Time series of weekly mean of VRP values from VIIRS ($VRP_{VIIRS}$) and SLSTR ($VRP_{SLSTR}$), in logarithmic scale, indicated respectively by crosses and circles. (b) Linear regression analyses between the weekly mean of $VRP_{VIIRS}$ and $VRP_{SLSTR}$ in logarithmic scale. The best-fit coefficient $m = 0.81$ indicates a good correlation between the time series of $VRP_{VIIRS}$ and $VRP_{SLSTR}$. For both the graphs, the colors in the range from blue to red indicate the values between January and December 2021, in chromatic order.

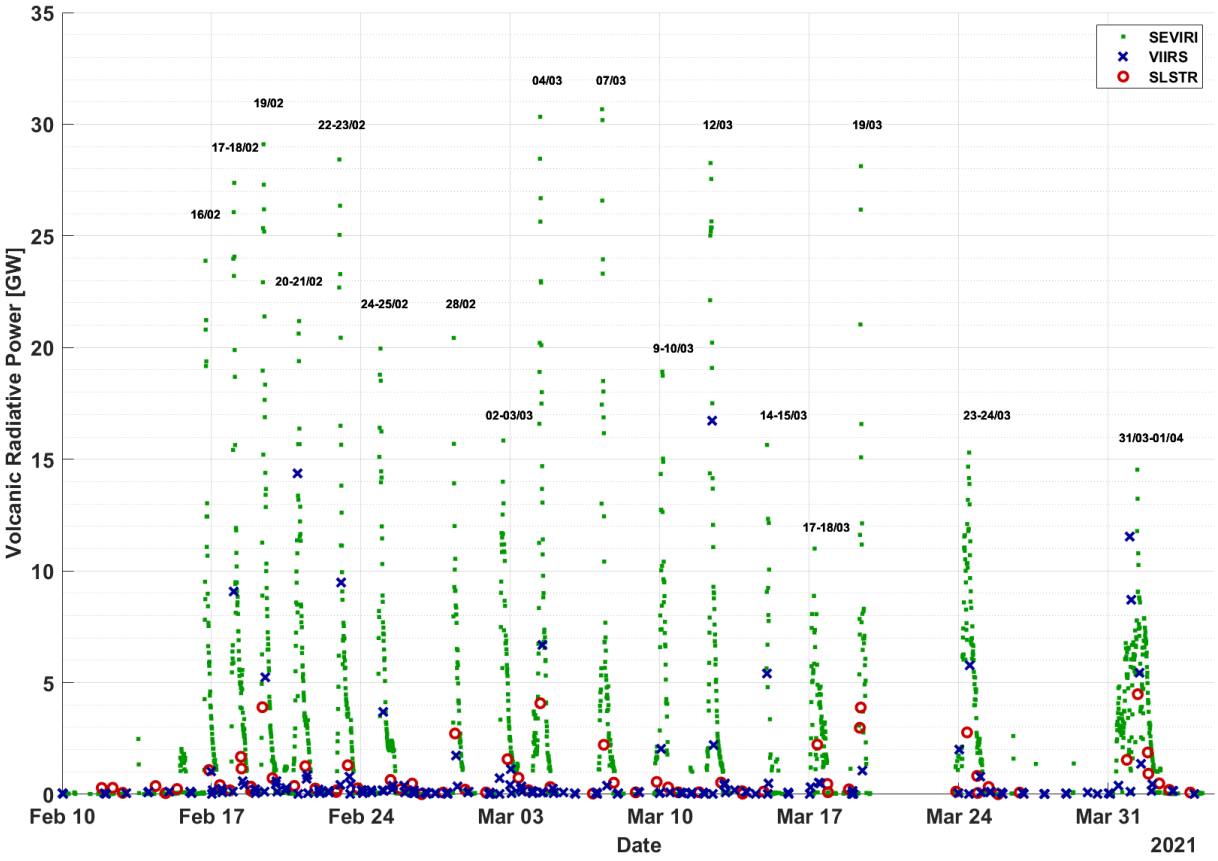


**Figure 5.** Temporal trend of VRP values derived from the Level-2 Products of VIIRS and SLSTR and estimated using SEVIRI data at 15 minutes' temporal resolution over the period 10 February – 4 April 2021 at Mt. Etna, during which 17 paroxysms occurred.

| Events | Interval time fitting SEVIRI [h] | τ from fitting SEVIRI ($\cdot 10^4$) | $f_{(0,SEVIRI)}$ from fitting SEVIRI [GW] | Estimation of $f_{(0,VIIRS)}$ [GW] | Estimation of $f_{(0,SLSTR)}$ [GW] | Estimation of $f_{(0,VIIRS\&SLSTR)}$ [GW] |
|---|---|---|---|---|---|---|
| 16 February 2021 | 17.50 | 1.13 | 22.85 | 8.96 (*) | 5.28 | 5.39 |
| 17-18 February 2021 | 21.00 | 1.56 | 23.88 | 9.26 | 9.77 | 9.77 |
| 19 February 2021 | 22.25 | 1.21 | 28.82 | 9.32 | 14.23 (*) | 9.27 |
| 20-21 February 2021 | 24.25 | 1.37 | 19.98 | 11.33 (*) | 10.44 | 9.9 |
| 22-23 February 2021 | 24.00 | 1.66 | 20.01 | 12.72 | 10.82 | 12.62 |
| 24-25 February 2021 | 23.00 | 1.39 | 18.18 | 7.52 (*) | 11.79 (*) | 7.95 |
| 28 February 2021 | 24.00 | 1.33 | 16.38 | 3.89 (*) | 4.21 | 4.01 |
| 2-3 March 2021 | 16.50 | 1.66 | 12.77 | 7.57 (*) | 4.41 (*) | 5.34 |
| 4 March 2021 | 18.75 | 1.13 | 29.59 | 13.67 (*) | 4.64 | 13.62 |
| 7 March 2021 | 24.25 | 0.95 | 31.26 | 2.78 (*) | 5.78 | 4.30 |
| 12 March 2021 | 22.50 | 1.21 | 30.37 | 28.14 (*) | 17.47 (*) | 27.63 |
| 23-24 March 2021 | 20.25 | 2.02 | 13.08 | 6.20 | 3.92 (*) | 5.67 |
| 31 March – 01 April 2021 | 26.25 | 3.72 | 10.48 | 6.92 (*) | 4.99 | 5.71 |

**Table 3.** Results obtained applying the procedure for the forecasting of thermal behavior of a lava fountain to thirteen paroxysmal events, occurred at Mt. Etna between February and April 2021.

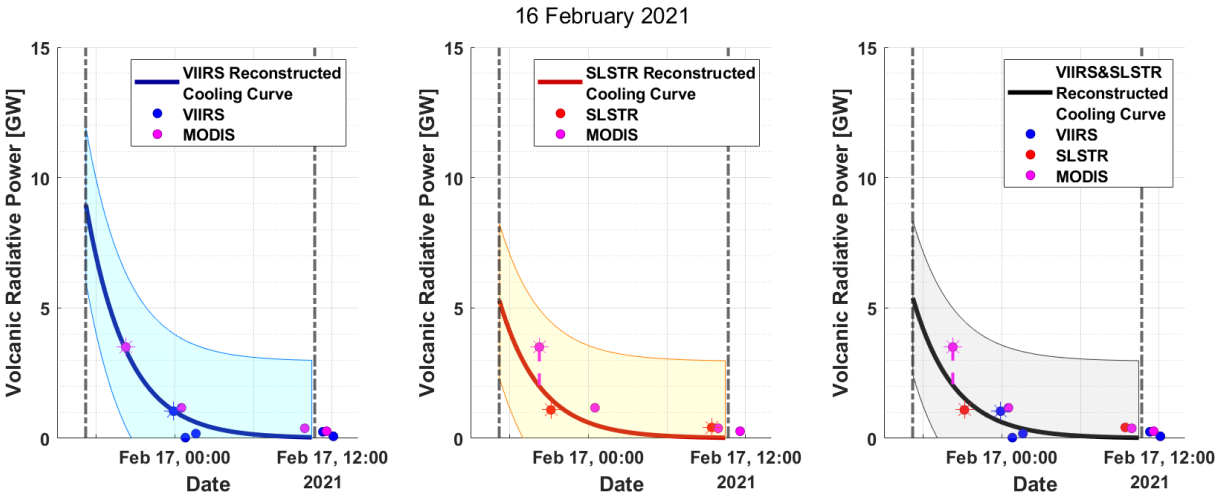


**Figure 6.** Reconstruction of the cooling curve from low temporal resolution VRP values, considering VIIRS data (6a), SLSTR data (6b) and together VIIRS and SLSTR data (6c) for the 16 February 2021 paroxysmal event. In magenta color, MODIS radiative power values used for the validation step.

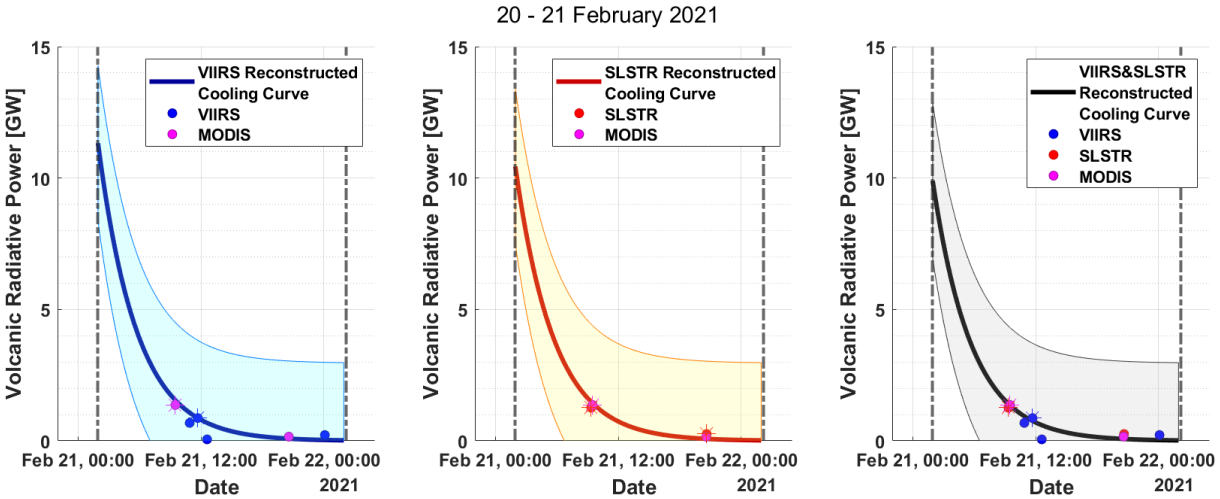


**Figure 7.** Reconstruction of the cooling curve from low temporal resolution VRP values, considering VIIRS data (7a), SLSTR data (7b) and together VIIRS and SLSTR data (7c) for the 20-21 February 2021 paroxysmal event. In magenta color, MODIS radiative power values used for the validation step.

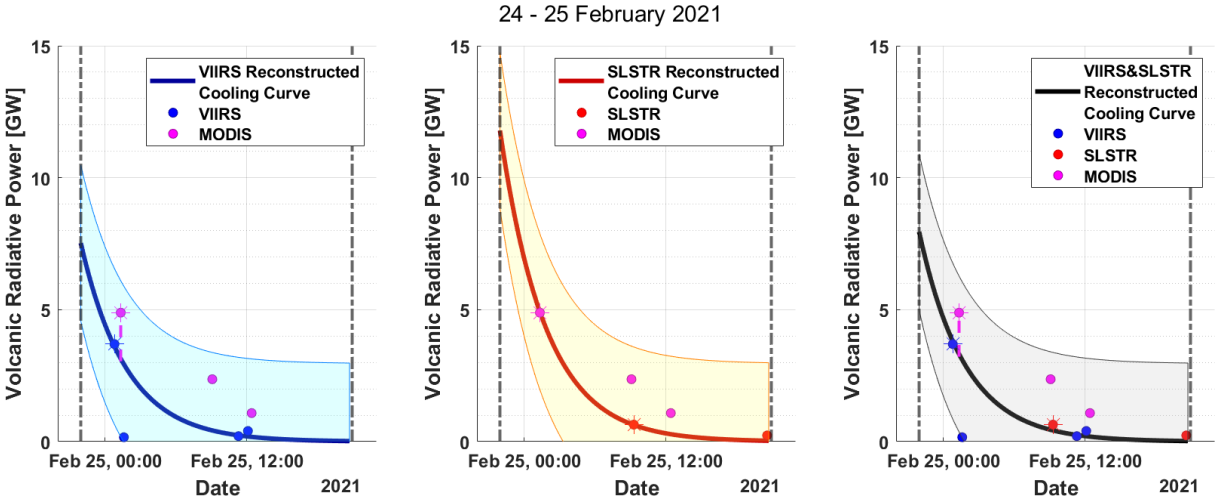


**Figure 8.** Reconstruction of the cooling curve from low temporal resolution VRP values, considering VIIRS data (8a), SLSTR data (8b) and together VIIRS and SLSTR data (8c) for the 24-25 February 2021 paroxysmal event. In magenta color, MODIS radiative power values used for the validation step.

volcanic activity, and the interval time chosen are the same adopted for SEVIRI fitting. In Figures 6-8, the asterisk points (blue for VIIRS and red for SLSTR) indicate the values taken into account to calculate the initial value.

Generally, two VRP values are used in order to make the calculation more robust, but if one of the two acquisitions is too far from the peak activity (like in Figure 8b for SLSTR) or assumes underestimated values near the peak of the activity (like in Figure 6a, Figure 7a and Figure 8a for VIIRS), only one VRP point is considered to estimate the initial value.

Figures 6-8 show the reconstructed cooling curve for each investigated event and a shaded area corresponding to the 95% confidence interval (CI) representing the uncertainty bound (in light blue for VIIRS, in yellow for SLSTR and in gray for VIIRS&SLSTR).

To validate the reconstructed synthetic data points, we compared them with the radiative power values from MODIS, retrieved from LAV@HAZARD. In particular, the MODIS radiative power values of each paroxysmal event analyzed were compared to temporally coincident radiative power values retrieved from the reconstructed cooling curve related to VIIRS, SLSTR and VIIRS&SLSTR. If these values are very close, it means that the process of

| Events | MODIS | | VIIRS | | SLSTR | | VIIRS&SLSTR | |
|---|---|---|---|---|---|---|---|---|
| | Acquisition time | VRP value [GW] | VRP reconstructed value [GW] | VRP difference with MODIS [GW] | VRP reconstructed value [GW] | VRP difference with MODIS [GW] | VRP reconstructed value [GW] | VRP difference with MODIS [GW] |
| 16 February 2021 | 16/02/2021 20:15 | 3.5 | 3.44 | 0.06 | 2.03 | 1.47 | 2.07 | 1.43 |
| 17-18 February 2021 | 18/02/2021 09:00 | 1.39 | 1.46 | 0.07 | 1.54 | 0.15 | 1.54 | 0.15 |
| 19 February 2021 | 19/02/2021 20:50 | 0.81 | 0.41 | 0.41 | 0.62 | 0.19 | 0.4 | 0.41 |
| 20-21 February 2021 | 21/02/2021 09:30 | 1.36 | 1.57 | 0.2 | 1.45 | 0.08 | 1.37 | 0.01 |
| 22-23 February 2021 | 23/02/2021 09:20 | 0.64 | 1.61 | 0.98 | 1.37 | 0.73 | 1.6 | 0.96 |
| 24-25 February 2021 | 25/02/2021 01:20 | 4.89 | 3.04 | 1.84 | 4.77 | 0.12 | 3.22 | 1.67 |
| 28 February 2021 | 28/02/2021 09:40 | 5.38 | 2.59 | 2.79 | 2.8 | 2.58 | 2.67 | 2.71 |
| 2-3 March 2021 | 03/03/2021 00:45 | 2.11 | 1.13 | 0.98 | 0.66 | 1.45 | 0.8 | 1.31 |
| 4 March 2021 | 04/03/2021 20:15 | 1.39 | 0.45 | 0.94 | 0.14 | 1.24 | 0.44 | 0.94 |
| 7 March 2021 | 07/03/2021 09:45 | 1.39 | 0.98 | 0.41 | 2.03 | 0.64 | 1.51 | 0.12 |
| 12 March 2021 | 12/03/2021 21:05 | 0.59 | 0.73 | 0.14 | 0.45 | 0.14 | 0.72 | 0.13 |
| 23-24 March 2021 | 24/03/2021 21:30 | 0.8 | 1.09 | 0.29 | 0.69 | 0.11 | 1 | 0.19 |
| 31 March – 01 April 2021 | 01/04/2021 12:55 | 6.24 | 4.59 | 1.65 | 3.31 | 2.93 | 3.78 | 2.46 |

**Table 4.** Comparison between the MODIS radiative power values of each paroxysmal event analyzed and the temporally coincident radiative power values retrieved from the reconstructed cooling curve related to VIIRS, SLSTR and VIIRS&SLSTR.

reconstruction of the cooling curves works well, since it can estimate radiative power even when the sensor does not acquire data.

In Figures 6-8, MODIS radiative power values considered for the validation step, respectively for the events of 16 February 2021, 20-21 February 2021, and 24-25 February 2021, are those represented in magenta color. In Table 4, the results of the validation step are reported. In particular, for each MODIS acquisition time is shown the corresponding estimated MODIS radiative power value, the radiative power values retrieved from the reconstructed cooling curve for VIIRS, SLSTR and VIIRS&SLSTR and the difference between these values and the MODIS radiative power value.

## 5. Discussion

The synergic use of VIIRS and SLSTR acquisitions allows to obtain a higher number of data with a good spatial resolution for the monitoring of thermal anomalies. The information content provided by the two sensors is in fact comparable as shown in Figure 4. The best-fit coefficient *m* equal to 0.81 confirms the strong correlation between the two datasets. The main difference lies in the increased ability of VIIRS to detect thermal anomalies even in periods of less intense volcanic activity, like the period September-December 2021, which was characterized just by 4 paroxysms (21 September 2021, 23 October 2021, 4 December 2021 and 15 December 2021). In this same period, SLSTR VRP values are less than those of VIIRS and are related mainly to the paroxysmal activity. On the other hand, since SLSTR has higher saturation temperature than VIIRS-I channel, i.e. higher radiative power, its trend is higher than VIIRS during most of the analyzed time interval. However, the high best-fit coefficient demonstrates that VIIRS and SLSTR are actually two comparable sensors with a similar sensitivity in the detection and quantification of high-temperature anomalies. Furthermore, the difference in the acquisition time allows to monitor volcanic events otherwise missed when using only one of the two satellite sensors. This is the case of the events occurred in May-June 2021 that have been monitored by SLSTR but missed by VIIRS.

The advantages of using FastVRP to monitor VRP are shown in Figure 5, in fact each lava fountain occurred on Etna from February to April 2021 is well described by combining information coming from VIIRS and SLSTR. Figure 5 shows that VIIRS provides relevant information especially about the paroxysm of 20-21 February and 12 March 2021, due to satellite overpass times matching to the time of the events. Results retrieved from VIIRS indicate that the 12 March 2021 paroxysms was the most intense in terms of radiative power, with values estimated around 17 GW (VIIRS image of 12 March 2021 at 10:48 UTC). This latter event was one of the most powerful and peculiar, because was accompanied by the formation of lava fountains which fed a very high eruptive column and an extensive ash plume [Calvari et al., 2021; Torrisi et al., 2022]. Marchese et al. [2021] investigated the Mt. Etna paroxysms of February-April 2021 and for the 12 March 2021 paroxysm indicated a lower value of radiative power, about 7 GW from MODIS observations. This difference is probably due to the fact that VIIRS provides a superior capability to detect smaller thermal anomalies respect to MODIS, with no notable dependence on view zenith angle [Li et al., 2018, 2020]. Sometimes VIIRS VRP showed lower values than MODIS VRP and this may be due to the presence of plume above the crater and the atmospheric absorption of carbon dioxide at VIIRS M13 band, used for VRP calculation [Fu et al., 2020]. During the 31 March – 1 April paroxysm, VRP retrieved from VIIRS data (~ 5.5 GW, VIIRS image of 1 April at 11:12 UTC) appeared underestimated compared to the temporally coincident MODIS observations (~ 14 GW, MODIS image of 1 April at 09:33 UTC – 14 GW), retrieved from Marchese et al. [2021]. This impact on VIIRS estimates could be caused by the volcanic plume and partial cloud cover above the crater.

Some synthetic initial VRP values $f_0$ from VIIRS and SLSTR appear particularly different and the main reason can be related to the smaller pixel area of VIIRS I-Bands. VIIRS which is able to discriminate thermal anomalies with a lower VRP than those identifiable with SLSTR [Xu et al., 2020]. Moreover, it is important to highlight that the two sensors observe the scenes at slightly different times and this means different conditions of the observed thermal anomaly and of the cloud coverage. This situation arises if we consider the 4 March and 12 March 2021 events. In these cases, the VRP values used for the forecasted procedure from VIIRS are higher than that from SLSTR, and therefore the synthetic initial VRP values $f_0$ from VIIRS (13.67 GW for the 4 March 2021 and 28.14 GW for the 12 March 2021) appear much greater than that of SLSTR (4.64 GW for the 4 March 2021 and 17.47 GW for the 12 March 2021).

The use of the fitting procedure allowed to exploit the temporal information provided by SEVIRI while keeping the higher accuracy given by VIIRS and SLSTR. This helps us dealing with the missing data points during fountain

cooling phases as shown in Figures 6-8. The main advantages of using SEVIRI data is the possibility of promptly detecting eruptive events. However, the low spatial resolution of SEVIRI could lead to omission errors, like the inability to detect thermal anomalies below a certain size and intensity [Freeborn et al., 2014]. Other factors impact on estimates of the radiative power from SEVIRI data, such as the atmospheric effects and the variation in retrieved thermal anomalies related to the subpixel location of the thermal anomaly with respect to the sensor instantaneous field of view (IFOV). These effects lead to a general underestimation of SEVIRI radiative power compared to the temporally coincident MODIS observations [Wooster et al., 2005; Roberts et al., 2005]. Moreover, the geometric resampling and the digital filter applied to SEVIRI raw data before to be available from EUMETSAT can underestimate the SEVIRI estimates of VRP [Wooster et al., 2015].

Nevertheless, SEVIRI could overestimate VRP due to the impact of Point Spread Function (PSF) on active fire detection. This effect is so large that even a small lava flow within a single pixel can generate significant effects on the measured radiance [Calle et al., 2009; Barnie & Oppenheimer, 2015].

We decided to combine polar and geostationary satellite sensor data to overcome the limits of each of them and exploit their strengths. VIIRS and SLSTR offer mid-high spatial resolution with which it is possible to spatially characterize eruptive phenomena and to retrieve accurate spatial information such as the areal extent of the volcanic thermal anomaly. On contrast, SEVIRI offers high temporal resolution capabilities and allows to get accurate temporal information of the monitored volcanic phenomena, such as the exponential decay factor of a lava fountain cooling curve. The combined use of these sensors is advantageous because it allows us to get more accurate radiative power estimation.

Reconstructed synthetic data points are coherent with the MODIS values that has been never used to reconstruct cooling curves but that fall inside the uncertainty band of the reconstructed curve. This provides a first proof of the validity of our approach for the cooling curve reconstruction. It is noticeable that the distance between the MODIS radiative power values and the corresponding radiative power values on the reconstructed cooling curves is always lower than the uncertainty value (see Table 4). It means that MODIS radiative power values are always within the 95% CI. In addition, there are cases where the distance is negligible, that is, the MODIS point is exactly on the cooling curves (e.g. 20-21 February 2021 paroxysm). These results highlight the correctness of the procedure for the reconstruction of the cooling curves and for the retrieval of the radiative power values related to VIIRS and SLSTR.

Although VIIRS and SLSTR acquire few points for each event, they show improvements in terms of VRP accuracy and sensitivity. In particular, they may either detect earlier the starting of a lava fountain event such as for the 20-21 February 2021 event (Figure 9a), i.e. VIIRS detects a peak on 21 February at 00:24 UTC due to the start of less intense lava fountain episodes from 00:00 UTC as documented in INGV weekly bulletins published at www.ct.ingv.it., or detect earlier subtle increases in VRP intensity such as for the 2 March 2021 eruption (Figure 9b), i.e. VIIRS detection occurs on 1 March at 23:24 UTC while SEVIRI on 2 March at 00:42 UTC.

The reconstruction procedure considering both VIIRS and SLSTR polar sensors permitted to forecast the cooling curves of the overall sequence of the lava fountains occurred at Etna between February-April 2021. VIIRS and SLSTR

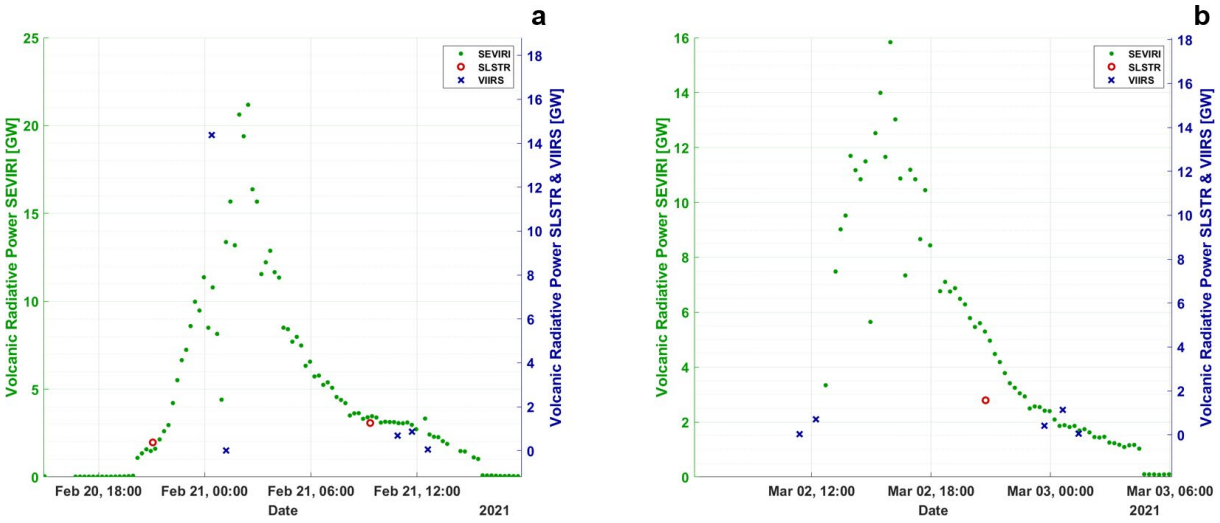


**Figure 9.** VRP monitored by VIIRS, SLSTR and SEVIRI for the events (a) 21 February 2021 and (b) 2 March 2021.

VRP values retrieved by FastVRP are exploited together with the SEVIRI data to apply the fitting procedure and then to reconstruct the cooling curves of the lava fountains sequence thanks to the retrieved synthetic data. Figure 10 shows the VRP values retrieved by FastVRP and reconstructed synthetic data using VIIRS and SLSTR (VIIRS&SLSTR). Although the acquisition frequency of VIIRS and SLSTR is low, it was possible to follow the thermal behavior of the lava fountains thanks to the temporal information provided by SEVIRI, maintaining the mid-high spatial accuracy of the two polar sensors.

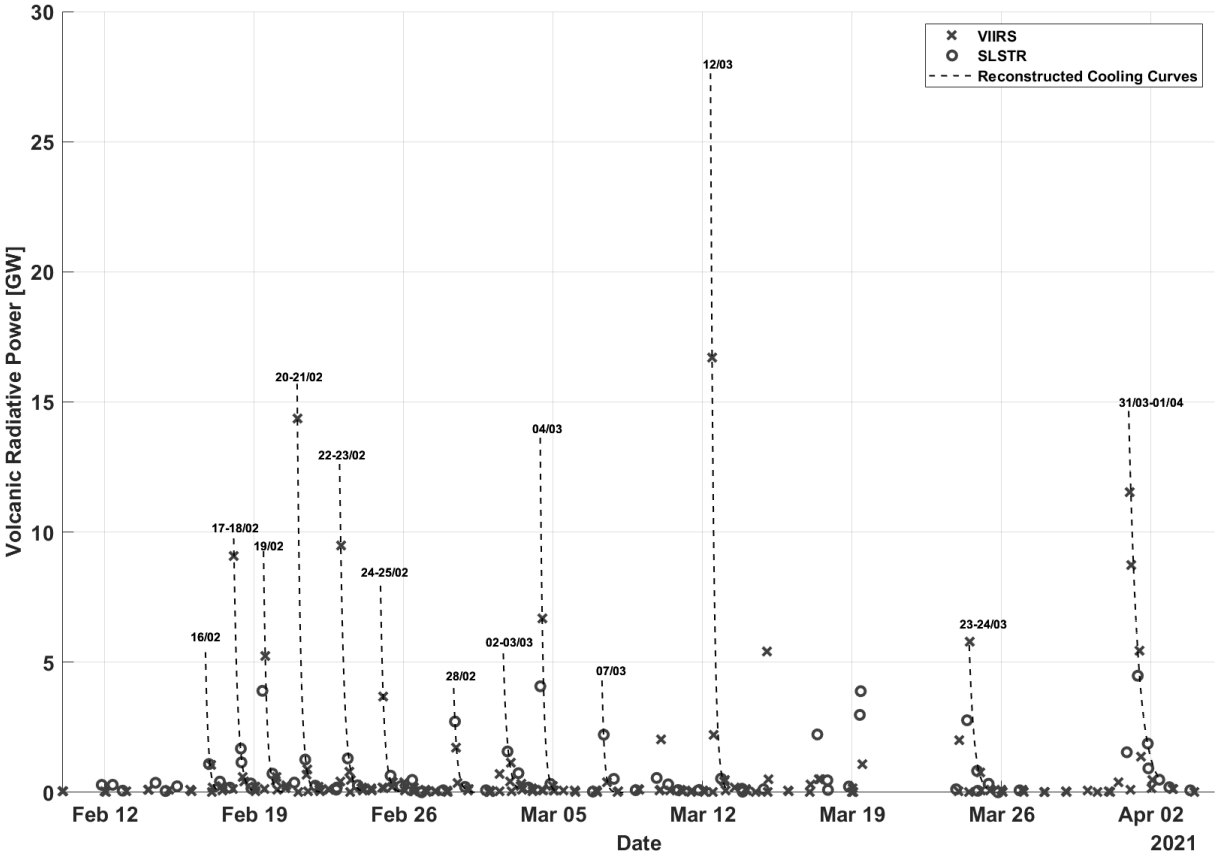


**Figure 10.** VRP values retrieved by FastVRP (markers) and reconstructed synthetic data using VIIRS and SLSTR (dashed line).

## 6. Conclusions

The FastVRP platform streamlines the retrievals of Level-2 FRP Products related to VIIRS and SLSTR sensors onboard polar satellites, provided respectively by NASA and ESA space agencies. FastVRP was implemented in Google Colab and allows to download automatically and process quickly both FRP Products, which can be used to monitor the volcanic thermal activity. Moreover, we proposed a novel approach to forecast the thermal behavior of a lava fountain with the synergic use of multi-sensor satellite data. This procedure is performed outside the Google Colab platform, but exploits the data provided by FastVRP. In particular, we combined the accurate spatial features provided by the polar satellite sensors VIIRS and SLSTR and the temporal features provided by the geostationary satellite sensor SEVIRI. This approach wants to improve and make more accurate the quality of the radiative power estimates.

This procedure was applied to the sequence of lava fountains occurred at Mt. Etna between February and April 2021. The VIIRS and SLSTR data were retrieved by the FastVRP platform, while SEVIRI radiative power estimates from LAV@HAZARD. The forecasting of thermal behavior of these lava fountains produced satisfactory results. The synthetic data obtained from VIIRS and SLSTR were used to reconstruct the cooling curves of each lava fountain, starting from the SEVIRI exponential decay calculated for each of these. The forecasted radiative values retrieved from the VIIRS and SLSTR cooling curves are close to the MODIS radiative power values (retrieved from LAV@

HAZARD), used as validation since MODIS has technical characteristics similar to those of the two sensors of interest. We have demonstrated that MODIS radiative power values are always within the 95% CI, therefore the VRP differences between the synthetic data and MODIS is lower than the uncertainty value (2.9 GW). Despite the few VRP values obtained from VIIRS and SLSTR due to their long revisit time, it was possible to monitor the thermal activity of the lava fountains even in the instants of time in which the two polar sensors do not acquire data, simply exploiting the temporal information provided by SEVIRI.

Furthermore, we evaluated the performance of VIIRS and SLSTR FRP Products. The linear regression analysis between the VIIRS and SLSTR VRP data confirms the correlation of the two datasets for the monitoring of volcanic thermal anomalies (best-fit coefficient m=0.81). Thus, we demonstrated that VIIRS and SLSTR FRP Products can be exploited to derive information about the thermal activity associated with the volcanic eruptions. The FastVRP platform can be a useful tool for near real-time monitoring of a volcanic activity. Moreover, the combined use of mid-high spatial resolution data offered by the VIIRS and SLSTR FRP Products and of high temporal resolution data provided by geostationary sensors like SEVIRI give us the possibility to forecast the thermal behavior of a lava fountain and then to get more accurate radiative power estimates.

**Funding.** This research was funded by [ATHOS Research Programme] (OB.FU. 0867.010) and by [Project FIRST – ForecastIng eRuptive activity at Stromboli volcano: timing, eruptive style, size, intensity, and duration, INGV – Progetto Strategico Dipartimento Vulcani 2019] (Delibera n. 144/2020).

**Acknowledgments.** This work was developed within the framework of the Laboratory of Technologies for Volcanology (TechnoLab) at the INGV in Catania (Italy). SLSTR and VIIRS Level-2 FRP Products used in this work are provided respectively by the European Space Agency and by NASA. Note: Google CoLaboratory™ is a trademark of Google LLC – ©2018 Google LLC All rights reserved.

## References

Alparone, S., D. Andronico, L. Lodato and T. Sgroi (2003). Relationship between tremor and volcanic activity during the Southeast Crater eruption on Mount Etna in early 2000, J. Geophys. Res.: Solid Earth, 108, B5, https://doi.org/10.1029/2002JB001866.

Amato, E., C. Corradino, F. Torrisi and C. Del Negro (2021). Mapping lava flows at Etna Volcano using Google Earth Engine, open-access satellite data, and machine learning. 2021 International Conference on Electrical, Computer, Communications and Mechatronics Engineering (ICECCME), 1-6, https://doi.org/10.1109/ICECCME52200.2021.9591110.

Amato, E. (2022). Machine learning and best fit approach to map lava flows from space. Il Nuovo Cimento C, 45, 4, 1-12, https://doi.org/10.1393/ncc/i2022-22080-1.

Andronico, D., A. Cannata, G. Di Grazia and F. Ferrari (2021). The 1986-2021 paroxysmal episodes at the summit craters of Mt. Etna: Insights into volcano dynamics and hazard, Earth-Sci. Rev., 220, 103686, https://doi.org/10.1016/j.earscirev.2021.103686.

Andronico, D. and P. Del Carlo (2016). $PM_{10}$ measurements in urban settlements after lava fountain episodes at Mt. Etna, Italy: pilot test to assess volcanic ash hazard to human health, Nat. Hazards Earth Sys. Sci., 16(1), 29-40. https://doi.org/10.5194/nhess-16-29-2016.

Andronico, D., S. Scollo, S. Caruso and A. Cristaldi (2008). The 2002-03 Etna explosive activity: Tephra dispersal and features of the deposits, J. Geophys. Res.: Solid Earth, 113, B4, https://doi.org/10.1029/2007JB005126.

Barnie, T. and C. Oppenheimer (2015). Extracting High Temperature Event radiance from satellite images and correcting for saturation using Independent Component Analysis, Remote Sens. Environ., 158, 56-68, https://doi.org/10.1016/j.rse.2014.10.023.

Behncke, B. and M. Neri (2003). The July-August 2001 eruption of Mt. Etna (Sicily), Bull.Volcanol., 65, 7, 461-476, https://doi.org/10.1007/s00445-003-0274-1.

Calle, A., J.-L. Casanova and F. González-Alonso (2009). Impact of point spread function of MSG-SEVIRI on active fire detection, Int. J. Remote Sens., 30, 17, 4567-4579, https://doi.org/10.1080/01431160802609726.

Calvari, S., A. Bonaccorso and G. Ganci (2021). Anatomy of a Paroxysmal Lava Fountain at Etna Volcano: The Case of the 12 March 2021, Episode, Remote Sensing, 13, 15, 3052, https://doi.org/10.3390/rs13153052.

Calvari, S. and G. Nunnari (2022). Comparison between Automated and Manual Detection of Lava Fountains from Fixed Monitoring Thermal Cameras at Etna Volcano, Italy, Remote Sensing, 14, 10, 2392, https://doi.org/10.3390/rs14102392.

Campus, A., M. Laiolo, F. Massimetti and D. Coppola (2022). The Transition from MODIS to VIIRS for Global Volcano Thermal Monitoring, Sensors, 22, 5, 1713, https://doi.org/10.3390/s22051713.

Cao, C., J. Xiong, S. Blonski, Q. Liu, S. Uprety, X. Shao, Y. Bai and F. Weng (2013). Suomi NPP VIIRS sensor data record verification, validation, and long-term performance monitoring, J. Geophys. Res.: Atmospheres, 118, 20, 11,664-11,678, https://doi.org/10.1002/2013JD020418.

Coppola, D., M. Laiolo, C. Cigolini, F. Massimetti, D. Delle Donne, M. Ripepe, H. Arias, S. Barsotti, C. B. Parra, R. G. Centeno, S. Cevuard, G. Chigna, C. Chun, E. Garaebiti, D. Gonzales, J. Griswold, J. Juarez, L. E. Lara, C. M. López, C. M., … R. William (2020). Thermal Remote Sensing for Global Volcano Monitoring: Experiences From the MIROVA System, Frontiers Earth Sci., 7, https://www.frontiersin.org/articles/10.3389/feart.2019.00362.

Corradino, C., E. Amato, F. Torrisi and C. Del Negro (2022). Data-Driven Random Forest Models for Detecting Volcanic Hot Spots in Sentinel-2 MSI Images, Remote Sensing, 14, 17, 4370, https://doi.org/10.3390/rs14174370.

Corradino, C., E. Amato, F. Torrisi, F. and C. Del Negro (2021). Towards an automatic generalized machine learning approach to map lava flows. 2021 17th International Workshop on Cellular Nanoscale Networks and Their Applications (CNNA), 1-4, https://doi.org/10.1109/CNNA49188.2021.9610813

Corradino, C., G. Bilotta, A. Cappello, L. Fortuna and C. Del Negro (2021). Combining Radar and Optical Satellite Imagery with Machine Learning to Map Lava Flows at Mount Etna and Fogo Island, Energies, 14, 1, 197, https://doi.org/10.3390/en14010197.

Corradino, C., G. Ganci, G. Bilotta, A. Cappello, C. Del Negro and L. Fortuna (2019). Smart Decision Support Systems for Volcanic Applications, Energies, 12, 7, 1216, https://doi.org/10.3390/en12071216.

Corradino, C., G. Ganci, A. Cappello, G. Bilotta, A. Hérault and C. Del Negro (2019). Mapping Recent Lava Flows at Mount Etna Using Multispectral Sentinel-2 Images and Machine Learning Techniques. Remote Sensing, 11, 16, 1916, https://doi.org/10.3390/rs11161916.

Davies, D., G. Ederer, O. Olsina, M. Wong, M. Cechini and R. Boller(2019, October 3). NASA's Fire Information for Resource Management System (FIRMS): Near Real-Time Global Fire Monitoring Using Data from MODIS and VIIRS, https://ntrs.nasa.gov/citations/20190032007

Di Bello, G., C. Filizzola, T. Lacava, F. Marchese, N. Pergola, C. Pietrapertosa, S. Piscitelli, I. Scaffidi and V. Tramutoli (2004). Robust satellite techniques for volcanicand seismic hazards monitoring, https://www.earth-prints.org/handle/2122/740

Flynn, L., R. Wright, H. Garbeil, A. Harris and E. Pilger (2002). A Global Thermal Alert System Using MODIS: Initial Results from 2000-2001, Adv. Environ. Monit. Mod., 1, 1, 37-60.

Freeborn, P. H., M. J. Wooster, G. Roberts and W. Xu (2014). Evaluating the SEVIRI Fire Thermal Anomaly Detection Algorithm across the Central African Republic Using the MODIS Active Fire Product, Remote Sensing, 6, 3, 1890-1917, https://doi.org/10.3390/rs6031890.

Fu, Y., R. Li, X. Wang, Y. Bergeron, O. Valeria, R. D. Chavardès, Y. Wang and J. Hu (2020). Fire Detection and Fire Radiative Power in Forests and Low-Biomass Lands in Northeast Asia: MODIS versus VIIRS Fire Products, Remote Sensing, 12, 18, 2870, https://doi.org/10.3390/rs12182870.

Ganci, G., G. Bilotta, A. Cappello, A. Herault and C. Del Negro (2016). HOTSAT: a multiplatform system for the thermal monitoring of volcanic activity using satellite data, Geol. Soc., London, Special Pub., 426, 1, 207-221, https://doi.org/10.1144/SP426.21.

Ganci, G., A. Cappello, G. Bilotta, A. Herault, V. Zago and C. Del Negro (2018). Mapping Volcanic Deposits of the 2011-2015 Etna Eruptive Events Using Satellite Remote Sensing, Frontiers Earth Sci., 6, https://www.frontiersin.org/articles/10.3389/feart.2018.00083.

Ganci, G., A. Harris, C. Del Negro, Y. Guehenneux, A. Cappello, P. Labazuy, S. Calvari and M. Gouhier (2012). A year of lava fountaining at Etna: Volumes from SEVIRI, Geophys. Res. Lett., 39, 6, https://doi.org/10.1029/2012GL051026.

Ganci, G., A. Vicari, A. Cappello and C. Del Negro (2012). An emergent strategy for volcano hazard assessment: From thermal satellite monitoring to lava flow modeling, Remote Sens. Environ., 119, 197-207, https://doi.org/10.1016/j.rse.2011.12.021.

Gouhier, M., Y. Guéhenneux, P. Labazuy, P. Cacault, J. Decriem and S. Rivet (2016). HOTVOLC: a web-based monitoring system for volcanic hot spots, Geol. Soc., London, Special Pub., 426, 1, 223-241, https://doi.org/10.1144/SP426.31.

Gunda, G. K. T., P. K. C. Ray, M. Chauhan, P. Chauhan and S. Balaji (2021). Barren Island volcanism and seismicity: An intriguing finding, J. Earth Sys. Sci., 130, 3, 162, https://doi.org/10.1007/s12040-021-01624-z

Harris, A. (2013). Thermal Remote Sensing of Active Volcanoes: A User's Manual, Cambridge University Press.

Harris, A. J. L., S. E. J. Swabey and J. Higgins (1995). Automated thresholding of active lavas using AVHRR data, Int. J. Remote Sens., 16, 18, 3681-3686, https://doi.org/10.1080/01431169508954654.

Higgins, J. and A. Harris (1997). VAST: A program to locate and analyse volcanic thermal anomalies automatically from remotely sensed data, Compu. Geosci., 23, 6, 627-645, https://doi.org/10.1016/S0098-3004(97)00039-3.

Hirn, B. R., C. Di Bartola, G. Laneve, E. Cadau, E. and F. Ferrucci (2008). SEVIRI Onboard Meteosat Second Generation, and the Quantitative Monitoring of Effusive Volcanoes in Europe and Africa. IGARSS 2008-2008 IEEE International Geoscience and Remote Sensing Symposium, 3, III-374-III-377, https://doi.org/10.1109/IGARSS.2008.4779361.

Li, F., X. Zhang and S. Kondragunta (2020). Biomass Burning in Africa: An Investigation of Fire Radiative Power Missed by MODIS Using the 375 m VIIRS Active Fire Product. Remote Sensing, 12, 1561, https://doi.org/10.3390/rs12101561.

Li, F., X. Zhang, S. Kondragunta and I. Csiszar (2018). Comparison of Fire Radiative Power Estimates From VIIRS and MODIS Observations, J. Geophys. Res.: Atmospheres, 123, 9, 4545-4563, https://doi.org/10.1029/2017JD027823.

Li, L., C. Solana, F. Canters and M. Kervyn (2017). Testing random forest classification for identifying lava flows and mapping age groups on a single Landsat 8 image, J. Volcanol. Geotherm. Res., 345, 109-124, https://doi.org/10.1016/j.jvolgeores.2017.07.014.

Lombardo, V., S. Corradini, M. Musacchio, M. Silvestri and J. Taddeucci (2019). Eruptive Styles Recognition Using High Temporal Resolution Geostationary Infrared Satellite Data, Remote Sensing, 11, 6, 669, https://doi.org/10.3390/rs11060669.

LP DAAC-VIIRS Overview. (n.d.). Retrieved October 13, 2022, from https://lpdaac.usgs.gov/data/get-started-data/collection-overview/missions/s-npp-nasa-viirs-overview/.

Marchese, F., C. Filizzola, T. Lacava, A. Falconieri, M. Faruolo, N. Genzano, G. Mazzeo, C. Pietrapertosa, N. Pergola, V. Tramutoli and M. Neri (2021). Mt. Etna Paroxysms of February-April 2021 Monitored and Quantified through a Multi-Platform Satellite Observing System, Remote Sensing, 13, 16, 3074, https://doi.org/10.3390/rs13163074.

Marchese, F., N. Genzano, M. Neri, A. Falconieri, G. Mazzeo and N. Pergola (2019). A Multi-Channel Algorithm for Mapping Volcanic Thermal Anomalies by Means of Sentinel-2 MSI and Landsat-8 OLI Data, Remote Sensing, 11, 23, 2876, https://doi.org/10.3390/rs11232876.

Massimetti, F., D. Coppola, M. Laiolo, S. Valade, C. Cigolini and M. Ripepe (2020). Volcanic Hot-Spot Detection Using SENTINEL-2: A Comparison with MODIS-MIROVA Thermal Data Series, Remote Sensing, 12, 5, 820, https://doi.org/10.3390/rs12050820.

Pergola, N., F. Marchese and V. Tramutoli (2004). Automated detection of thermal features of active volcanoes by means of infrared AVHRR records, Remote Sens. Environ., 93, 3, 311-327, https://doi.org/10.1016/j.rse.2004.07.010.

Piscini, A. and V. Lombardo (2014). Volcanic hot spot detection from optical multispectral remote sensing data using artificial neural networks, Geophys. J. Int., 196, 3, 1525-1535, https://doi.org/10.1093/gji/ggt506.

Roberts, G., M. J. Wooster, G. L. W. Perry, N. Drake, L.-M. Rebelo and F. Dipotso (2005). Retrieval of biomass combustion rates and totals from fire radiative power observations: Application to southern Africa using geostationary SEVIRI imagery, J.. Geophys. Res.: Atmospheres, 110, D21, https://doi.org/10.1029/2005JD006018.

Schroeder, W., P. Oliva, L. Giglio and I. A. Csiszar (2014). The New VIIRS 375m active fire detection data product: Algorithm description and initial assessment, Remote Sens. Environ., 143, 85-96, https://doi.org/10.1016/j.rse.2013.12.008.

Sentinel-3 – Mission Summary – Sentinel Online – Sentinel Online. (n.d.). Retrieved October 7, 2022, from https://sentinels.copernicus.eu/web/sentinel/missions/sentinel-3/overview/mission-summary.

Torrisi, F., E. Amato, C. Corradino, S. Mangiagli and C. Del Negro (2022). Characterization of Volcanic Cloud Components Using Machine Learning Techniques and SEVIRI Infrared Images, Sensors, 22, 20, 7712. https://doi.org/10.3390/s22207712.

Torrisi, F., F. Folzani, C. Corradino, E. Amato and C. Del Negro (2022, January 5). Detecting Volcanic Ash Plume Components from Space using Machine Learning Techniques (world) [Poster]. Earth and Space Science Open Archive; Earth Space Sci. Open Arch, https://doi.org/10.1002/essoar.10509947.1.

Torrisi, F. (2022). Automatic detection of volcanic ash clouds using MSG-SEVIRI satellite data and machine learning techniques, Il Nuovo Cimento C, 45, 4, 1-10, https://doi.org/10.1393/ncc/i2022-22081-0.

Tramutoli, V. (1998). Robust AVHRR techniques (RAT) for environmental monitoring: theory and applications, Earth Surf. Remote Sens. II, 3496, 101-113, https://doi.org/10.1117/12.332714.

Valade, S., A. Ley, F. Massimetti, O. D'Hondt, M. Laiolo, D. Coppola, D. Loibl, O. Hellwich and T. R. Walter (2019). Towards Global Volcano Monitoring Using Multisensor Sentinel Missions and Artificial Intelligence: The MOUNTS Monitoring System, Remote Sensing, 11, 13, 1528, https://doi.org/10.3390/rs11131528.

Vicari, A., G. Bilotta, S. Bonfiglio, A. Cappello, G. Ganci, A. Hérault, E. Rustico, G. Gallo and C. Del Negro (2011). LAV@HAZARD: a web-GIS interface for volcanic hazard assessment, Ann. Geophys., 54, 5, Article 5, https://doi.org/10.4401/ag-5347.

Wooster, M. J., G. Roberts, P. H. Freeborn, W. Xu, Y. Govaerts, R. Beeby, J. He, A. Lattanzio, D. Fisher and R. Mullen (2015). LSA SAF Meteosat FRP products – Part 1: Algorithms, product contents, and analysis, Atmospheric Chemistry and Physics, 15, 22, 13217-13239, https://doi.org/10.5194/acp-15-13217-2015.

Wooster, M. J., G. Roberts, G. L. W. Perry and Y. J. Kaufman (2005). Retrieval of biomass combustion rates and totals from fire radiative power observations: FRP derivation and calibration relationships between biomass consumption and fire radiative energy release, J. Geophys. Res.: Atmospheres, 110, D24, https://doi.org/10.1029/2005JD006318.

Wooster, M. J., W. Xu and T. Nightingale (2012). Sentinel-3 SLSTR active fire detection and FRP product: Pre-launch algorithm development and performance evaluation using MODIS and ASTER datasets. Remote Sens. Environ., 120, 236-254, https://doi.org/10.1016/j.rse.2011.09.033.

Wooster, M. J., B. Zhukov and D. Oertel (2003). Fire radiative energy for quantitative study of biomass burning: derivation from the BIRD experimental satellite and comparison to MODIS fire products. Remote Sens. Environ., 86, 1, 83-107, https://doi.org/10.1016/S0034-4257(03)00070-1.

Wright, R., L. Flynn, H. Garbeil, A. Harris and E. Pilger (2002). Automated volcanic eruption detection using MODIS, Remote Sens. Environ., 82, 1, 135-155, https://doi.org/10.1016/S0034-4257(02)00030-5.

Wright, R., L. P. Flynn, H. Garbeil, A. J. L. Harris and E. Pilger (2004). MODVOLC: near-real-time thermal monitoring of global volcanism, J. Volcanol. Geotherm. Res., 135, 1, 29-49, https://doi.org/10.1016/j.jvolgeores.2003.12.008.

Xu, W., M. J. Wooster, J. He and T. Zhang (2020). First study of Sentinel-3 SLSTR active fire detection and FRP retrieval: Night-time algorithm enhancements and global intercomparison to MODIS and VIIRS AF products, Remote Sens. Environ., 248, 111947, https://doi.org/10.1016/j.rse.2020.111947.

Xu, W., M. J. Wooster, E. Polehampton, R. Yemelyanova and T. Zhang (2021). Sentinel-3 active fire detection and FRP product performance – Impact of scan angle and SLSTR middle infrared channel selection, Remote Sens. Environ., 261, 112460, https://doi.org/10.1016/j.rse.2021.112460.

Zhang, T., M. J. Wooster and W. Xu (2017). Approaches for synergistically exploiting VIIRS I- and M-Band data in regional active fire detection and FRP assessment: A demonstration with respect to agricultural residue burning in Eastern China, Remote Sens. Environ., 198, 407-424, https://doi.org/10.1016/j.rse.2017.06.028.

***CORRESPONDING AUTHOR: Federica TORRISI**,
Istituto Nazionale di Geofisica e Vulcanologia, Osservatorio Etneo – Sezione di Catania, Catania, Italy
and Department of Electrical, Electronic and Computer Engineering, University of Catania,Catania, Italy
e-mail: federica.torrisi@ingv.it